Status of the TRMM 2A12 Land Precipitation Algorithm

KAUSHIK GOPALAN AND NAI-YU WANG

Earth System Science Interdisciplinary Center, University of Maryland, College Park, College Park, Maryland

RALPH FERRARO

NOAA/NESDIS/Center for Satellite Applications and Research (STAR)/SCSB, Camp Springs, and Cooperative Institute of Climate Studies, ESSIC, University of Maryland, College Park, College Park, Maryland

CHUNTAO LIU

Department of Atmospheric Sciences, University of Utah, Salt Lake City, Utah

(Manuscript received 2 February 2010, in final form 8 April 2010)

ABSTRACT

This paper describes improvements to the Tropical Rainfall Measurement Mission (TRMM) Microwave Imager (TMI) land rainfall algorithm in version 7 (v7) of the TRMM data products. The correlations between rain rates and TMI 85-GHz brightness temperatures (Tb) for convective and stratiform rain are generated using 7 years of collocated TMI and TRMM precipitation radar (PR) data. The TMI algorithm for estimating the convective ratio of rainfall is also modified. This paper highlights both the improvements in the v7 algorithm and the continuing problems with the land rainfall retrievals. It is demonstrated that the proposed changes to the algorithm significantly lower the overestimation by TMI globally and over large sections of central Africa and South America. Also highlighted are the problems with the 2A12 land algorithm that have not been addressed in the version 7 algorithm, such as large regional and seasonal dependence of biases in the TMI rain estimates, and potential changes to the algorithm to resolve these problems are discussed.

1. Introduction

The Tropical Rainfall Measurement Mission (TRMM) Microwave Imager (TMI), a nine-channel (10–85 GHz) dual-polarized microwave radiometer, is one of five instruments aboard the TRMM spacecraft and is used to provide rainfall estimates over the tropics. The TRMM 2A12 data product, which contains instantaneous rainfall estimates from TMI, uses separate algorithms for land, ocean, and coastal regions. Separate algorithms are required for these three cases because of the major differences in the microwave emission characteristics of each surface type. The ocean surface is radiometrically cold and strongly polarized at microwave frequencies at low and moderate wind speeds; hence, the warm, randomly polarized emission from rainfall can be easily distinguished from the ocean surface emission. In contrast, land surfaces are radiometrically warm and highly unpolarized; therefore, the depression in the 85-GHz brightness temperature (Tb) from ice scattering is primarily used to estimate rainfall over land. Further, land surfaces are typically highly nonhomogeneous and can have extremely variable surface emissivities. Thus, the TMI land rainfall algorithm has traditionally been implemented through empirically derived Tb–rain-rate relationships, rather than relying on the physically based radiative transfer modeling of rainfall (as is the case with the TMI ocean algorithm). This paper details the improvements made to the TMI land rainfall algorithm in preparation for version 7 of the TRMM 2A12 data product, which were developed based on empirical analysis of a multiyear global set of collocations between TMI and the precipitation radar (PR). However, there are ongoing efforts in the satellite retrieval community aiming to characterize the land surface emissivity, and it is expected that future versions of the TMI land algorithm will be more physically based.

Corresponding author address: Kaushik Gopalan, Earth System Science Interdisciplinary Center, University of Maryland, College Park, 5825 University Research Ct. Ste. 4001, College Park, MD 20740.
E-mail: kaushik@umd.edu

DOI: 10.1175/2010JTECHA1454.1

The TMI land rainfall algorithm was originally developed for the Special Sensor Microwave Imager (SSM/I) and was based on an empirically derived scattering index using the 19-, 22-, and 85-GHz vertically polarized channels (Grody 1991). The version 5 algorithm estimated the surface rainfall as a function of the scattering index; this function was derived using SSM/I collocations with ground radar over the United States, the United Kingdom, and Japan (Ferraro and Marks 1995). The TMI algorithm was then significantly restructured in version 6 (v6) of the TMI rain product. The near-surface rain rates (RRs) were estimated as a function of the 85-GHz vertically polarized Tb values (85V Tb), as described by McCollum and Ferraro (2003). The 85V Tb–RR relationship was derived empirically by using collocations between TMI and the PR over Africa and South America from October and November 2000. Separate Tb–RR relationships were derived for different storm types; that is, for stratiform and convective storms. These Tb–RR relationships were incorporated into the Goddard profiling (GPROF) framework (Kummerow et al. 2001) by extracting a set of profiles that follow the empirically derived 85V Tb–RR relationships and using these profiles to estimate near-surface rain rates from Tb observations using a Bayesian framework. The RR estimates for stratiform and convective storms are combined for each pixel using a convective probability indicator using the following equation:

$$\mathrm{RR} = \mathrm{RR}_{\mathrm{conv}} P(C) + \mathrm{RR}_{\mathrm{strat}}[1 - P(C)], \qquad (1)$$

where RR is the TMI v6 rain-rate estimate, $\mathrm{RR}_{\mathrm{conv}}$ is the RR estimated from the convective profiles, $\mathrm{RR}_{\mathrm{strat}}$ is the RR estimated from the stratiform profiles, and $P(C)$ is the TMI estimate of the convective probability (ratio) of the observed rainfall. Here, $P(C)$ is estimated using a linear combination of the following seven predictors (McCollum and Ferraro 2003): the vertically polarized brightness temperatures from 10-, 37-, and 85-GHz channels; the spatial standard deviation of the 85V Tb over a 40 km × 40 km area (from Grecu and Anagnostou 2001); the brightness temperature minima as developed by Prabhakara et al. (2000); and, last, the polarization difference and the normalized polarization difference at 85 GHz (from Olson et al. 2001).

Comparisons of the TMI v6 land rainfall estimates with rain-rate estimates from other sources have revealed some significant anomalies in these estimates. The TMI estimates were found to be higher than rain estimates from both PR and the Global Precipitation Climatology Project (GPCP), as described by Wang et al. (2009). This overestimation of rainfall by TMI is most prominent over central Africa and Tibet. TMI is also known to underestimate "warm" rainfall over land (Liu and Zipser 2009) because of the lack of significant ice scattering in such rainfall. Further, the RR biases between TMI and both PR and GPCP were observed to have strong seasonal variations. These inconsistencies in the TMI land retrievals are a serious concern to the users of these retrievals.

The work described in this paper focuses on reducing the overestimation of the global mean rainfall over land by TMI by developing a more robust model of the TMI RR–85V Tb relationship. This is accomplished by using a more comprehensive training set of collocations between TMI and PR than that of v6, which was trained using TMI–PR collocations from October and November 2000. In this work we use TMI–PR land collocations extending globally (excluding the higher latitudes that are not covered by TRMM) from 2002 to 2008, that is, almost the entire duration of the TRMM mission since the orbit boost in late 2001. The TMI–PR collocations were obtained from the University of Utah TRMM precipitation and cloud feature database (Liu et al. 2008). Similar modeling of the TMI land rain rates, assuming polynomial RR–Tb relationships, was performed by Dinku and Anagnostou (2005), who performed their analysis on four regions (central Africa, the Amazon, the U.S. southern plains, and the Ganga–Brahmaputra–Meghna River basin) for the summer seasons in 2000–02. PR rain rates from specific regions and limited time periods have also been used as a training set by McCollum and Ferraro (2003) and Grecu and Anagnostou (2001). This paper builds on the previous work by McCollum and Ferraro (2003) by taking advantage of the vastly expanded training set of TMI–PR collocations that has become available since the release of the TMI v6 algorithm, and using them to significantly reduce the biases in the global TMI rainfall estimates.

2. Methodology

The University of Utah level 1 Precipitation Feature (PF) database provides collocations between TMI and PR pixels for every TRMM orbit for the 7-yr period from January 2002 to December 2008. The PF database assigns a TMI pixel at the 85-GHz resolution as the "nearest neighbor" for every PR pixel in an orbit. Because of the finer sampling in PR as compared to TMI, there are typically from three to four PR pixels assigned as the nearest neighbor to every TMI pixel within the PR swath. To generate the training dataset, the PR near-surface rain rates (Iguchi et al. 2000) of all of the pixels corresponding to a given TMI pixel were averaged to give the "apparent" RR for that given pixel. This RR estimate was stored along with all of the TMI Tb measurements for every TMI high-resolution (85 GHz) pixel.

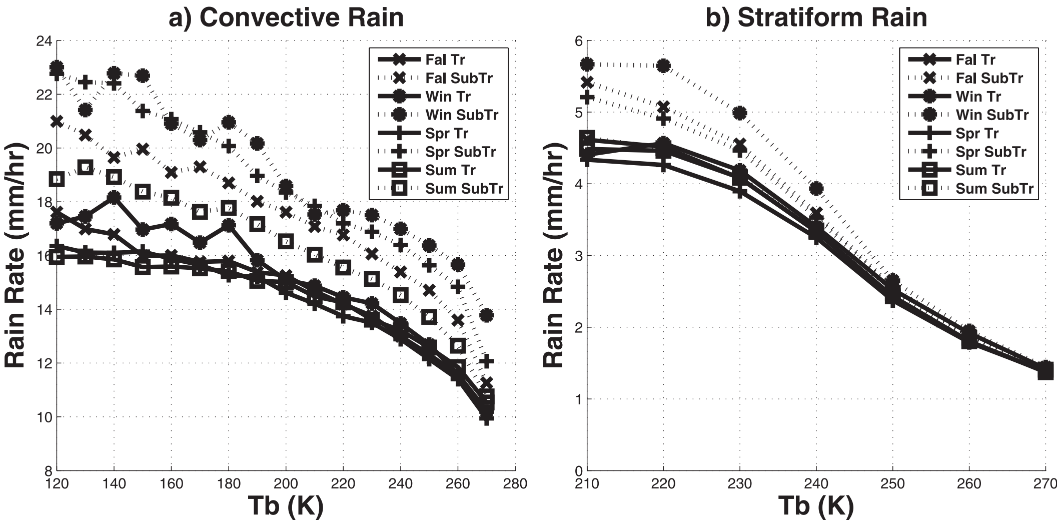

FIG. 1. Mean PR RR for 10-K TMI 85V Tb bins for different seasons and latitude ranges for (a) convective and (b) stratiform pixels. There are significant differences in the RR–Tb relationships in the tropics and the subtropics. The RR–Tb relationships for different seasons are also significantly different in the subtropics.

The sampling rates for the TMI 10–37-GHz channels are half that of the 85-GHz channels in the along-scan direction; thus, these low-resolution Tb values are interpolated appropriately to align them with the TMI 85-GHz measurements. The PR classification of the storm type from the TRMM 2A23 data product was also included in this dataset. This training dataset was then filtered to only include those TMI pixels that are tagged as ''land'' pixels in the 2A12 data product (pixels tagged as ''coast'' are also excluded).

The PF database corrects for the difference in the view angles of PR and TMI by implementing a parallax correction that consists of shifting the TMI observations back (forward) by one scan for the forward 0° (180°) yaw orientation for TMI. This correction is optimized for deep convective clouds; it is not suited for the most shallow storms, which constitute a large fraction of the precipitation observed by TRMM. Therefore, this correction was canceled for the purpose of this work by shifting the TMI observations in the PF database back to their original locations. Section 2a describes the procedure used to generate the PR RR–TMI 85V Tb relationships using the modified collocations from the PF database.

a. *Generation of PR RR–TMI 85V Tb relationships for convective and stratiform storms*

The first step of our empirical analysis was to examine the RR–85V Tb relationships of convective and stratiform rainfall separately. The PR 2A23 rain-type flag (Awaka et al. 1998) was used for this purpose. Those TMI pixels for which 75% or greater of the associated PR pixels were tagged as ''convective certain'' were used to generate the RR–Tb curve for convective rain, and a similar procedure was used for stratiform rain. When the mean PR RR of a bin size of 10 K from 85V Tb in the range of 120–270 K for both convective and stratiform storms from January 2002–December 2008 were calculated, a clear distinction was observed between the RR–Tb relationships for convective and stratiform storms, as was expected. Further, the data were separated into four seasons (spring, summer, fall, and winter) and two latitude bins, the tropics (between 20°N and 20°S) and the subtropics (north of 20°N and south of 20°S), in order to observe the regional and seasonal variations in the TMI Tb–RR relationships. Significant differences were observed in the Tb–RR relationships of the seasonal/latitude regimes, as shown in Fig. 1. The RRs for each Tb bin were found to be generally higher in the subtropics than in the tropics for all seasons. The differences in the Tb–RR relationships for different seasons were relatively small in the tropics, while they were significantly larger (up to $\approx$5 mm h^{-1} for each Tb bin) in the subtropics, which have more seasonal variability in storm types than the tropics.

These significant differences in the Tb–RR relationships for the different seasonal/latitude regimes seemed to be a promising indicator that our approach would help reduce the seasonal and geographic variability of the TMI RR biases. However, the maximum mean RR for convective storms saturated at approximately 20 mm h^{-1} for all of the seasonal and latitude regimes. Such a low value of the maximum estimated rainfall is extremely unrealistic and would render the TMI RR product unusable for many applications. It was also observed that the minimum mean RR for stratiform storms was $\approx$1.5 mm h^{-1}.

These problems were addressed using the filtering mechanism described in section 2b.

b. Filtering the TMI–PR dataset

To understand the saturation of the mean RRs at the high end for convective pixels and the low end for stratiform, the distribution of the apparent PR RRs for the different Tb bins were analyzed closely. For convective storms, it was discovered that a significant fraction of the low Tb pixels in the TMI–PR collocation set had a very low value of the ''apparent'' RR estimated by PR. There is strong 85V Tb depression in these pixels that is apparently not caused by rain, but perhaps by surface scattering (over snow-covered and arid lands). These pixels cannot be accurately represented by the current TMI land algorithm, whose accuracy depends greatly on the assumed relationship between the negative ''ice scattering'' signal observed in the 85V channel Tb and surface RR, because the assumed 85V Tb–RR correlation is clearly not true for these pixels. These anomalous points cause the saturation of the maximum estimated RR at an unrealistically low value for convective pixels. Conversely, for some stratiform pixels, there is no discernible 85V Tb depression even though the PR apparent RR is significantly high. These occurrences are likely during ''warm rain,'' where there is not sufficient ice in the atmosphere to cause a Tb depression in the 85V channel.

To combat the challenges described above, a filtering method was designed to remove pixels with significant surface scattering signatures from the convective training set, and to remove pixels with warm rainfall that is undetectable by the current TMI algorithm from the stratiform training set. A heuristic method based on the PR and TMI v6 rain rates was used to filter the training dataset. It was assumed that gross errors between TMI v6 and PR RRs are caused by fundamental limitations in the TMI algorithm that cannot be solved simply by developing a more robust estimate of the TMI RR–Tb relationship and would require more fundamental changes in the algorithm structure. Thus, pixels that exhibited such gross errors were treated as ''outliers'' and excluded from the training dataset. The pixels where the TMI v6 RR was higher than the PR RR by 50% or more were excluded from the convective training set and the pixels where the TMI v6 RR was lower than the PR RR by 50% or more were excluded from the stratiform training set.

The threshold of 50% was determined experimentally and was chosen to provide a reasonable balance between discarding the minimum number of points (which requires the threshold to be as high as possible) and minimizing the effect of the ''outliers'' on the Tb–RR regressions (which requires the threshold to be low). Using this method, approximately 30% of the points in the convective dataset and 5% of the points in the stratiform dataset were excluded. The geographic distribution of the discarded pixels for the June–August (JJA) and December–February (DJF) seasons for both the convective and stratiform storms is shown in Fig. 2. In JJA, the majority of discarded convective pixels are concentrated around the semiarid regions and grasslands in Africa, the mountainous regions of southeast and central Asia, and the southern United States. It is likely that TMI overestimates RR in semiarid regions because of surface scattering. Some of the excluded pixels are over the center of deep convective cores with large ice scattering and extremely cold Tb, but the PR near-surface reflectivity values over these pixels are not as high, possibly resulting from attenuation. Subcloud evaporation of rain is also a likely cause of the RR overestimation by TMI over semiarid regions. In this case, the liquid hydrometeors evaporate before reaching the surface and do not contribute to the near-surface precipitation. Additionally, the differences in the TMI and PR observations may also be caused by the large difference in the viewing angle of the two instruments. These differences are especially significant for deep convective rainfall, which makes up the bulk of the excluded pixels. Over the mountainous regions in Asia, the Appalachian Mountains, the Rocky Mountains, and the Sierra Nevada, neither TMI nor PR are likely to be completely accurate. In DJF, there is a high percentage of discarded pixels in southern Africa and South America. Much of the precipitation in these areas comes from storms with deep convective cores, over which both TMI and PR have occasional problems obtaining accurate rain estimates. The collocation of TMI and PR RR estimates is also problematic over such deep convection. Thus, these pixels are excluded from the training dataset used to generate the TMI Tb–RR relationship.

After filtering the dataset, the convective RR–Tb curve (estimated using mean PR RRs for 10-K 85V Tb bins) no longer saturates at the lower Tb values and the mean PR RR continues to increase beyond $\approx$45 mm h^{-1} when the 85V Tb goes below 120 K (see Fig. 3a). The minimum PR RR for the stratiform curves also goes down to $\approx$1 mm h^{-1} after filtering, as is shown in Fig. 3b. The filtering technique also removes the differences between the different seasonal/latitude bins; the differences between the Tb and RR relationships for the eight different regimes are negligibly small. This implies that the main regional and seasonal Tb–RR differences shown in Fig. 1 are due to warm rainfall, the extreme deep convective core, and surface emission contamination. Without considering these situations, a general Tb–RR relationship may apply well to most precipitation systems in different seasons and over various regions.

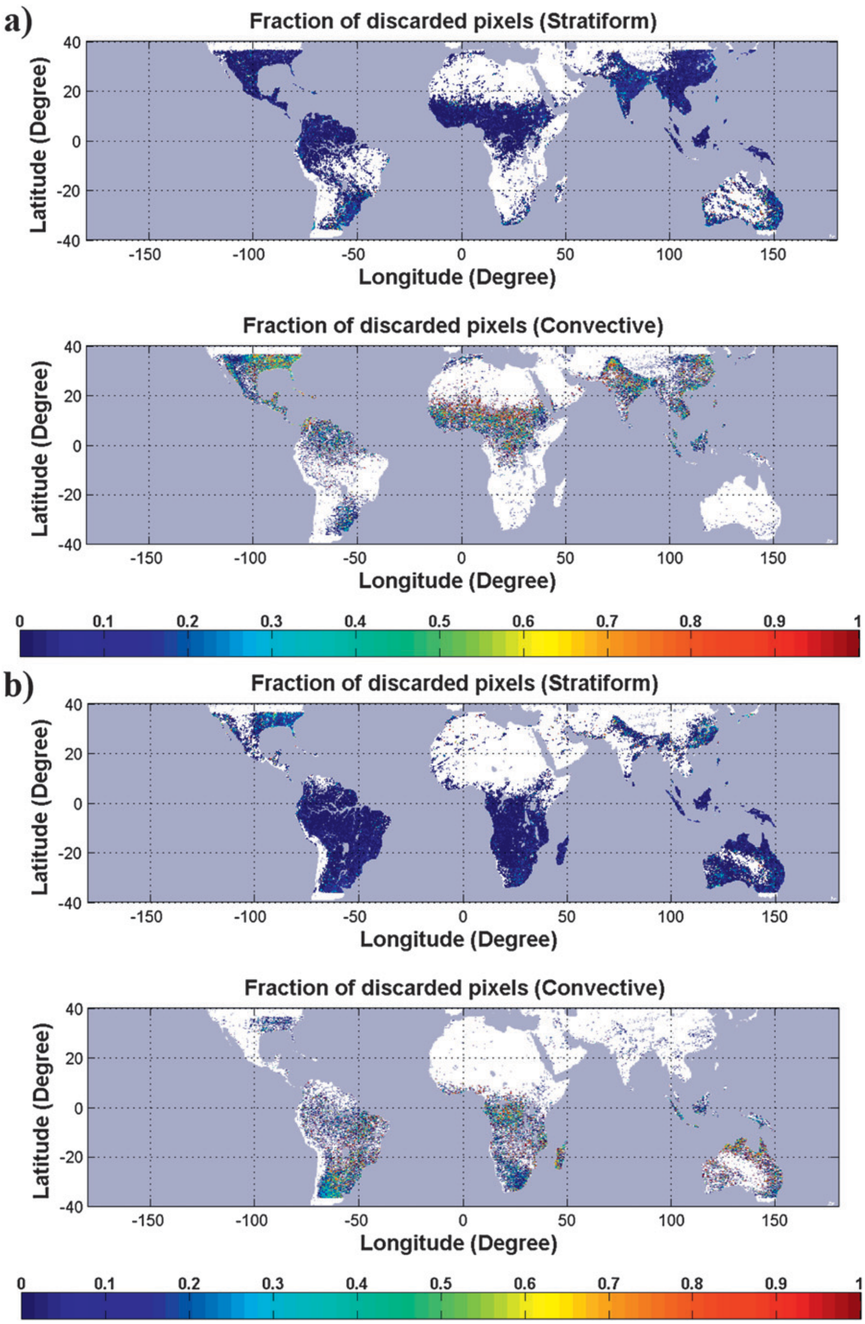

FIG. 2. Geographic distribution of the fraction of pixels discarded by the filtering algorithm in (a) JJA and (b) DJF.

The PR RR–85V Tb relationships were modeled by applying a polynomial fit to the mean PR values for TMI 85V Tb bins from 120 to 270 K (with 10-K width for each bin) for convective pixels, using a single fit globally for all seasons. Only the Tb bins from 210 to 270 K were used to generate the stratiform model because there were very few pixels with stratiform rain and Tb values below 210 K. A cubic RR–Tb model was used for convective storms while a linear model was used for stratiform storms, as shown below,

$$\mathrm{RR}_{\mathrm{conv}} = -0.000\,011\,77\mathrm{Tb}_{85\mathrm{V}}^{3} + 0.008\,027\mathrm{Tb}_{85\mathrm{V}}^{2} + -1.946\mathrm{Tb}_{85\mathrm{V}} + 182.68 \qquad (2)$$

$$\mathrm{RR}_{\mathrm{strat}} = -0.0708\mathrm{Tb}_{85\mathrm{V}} + 19.7, \qquad (3)$$

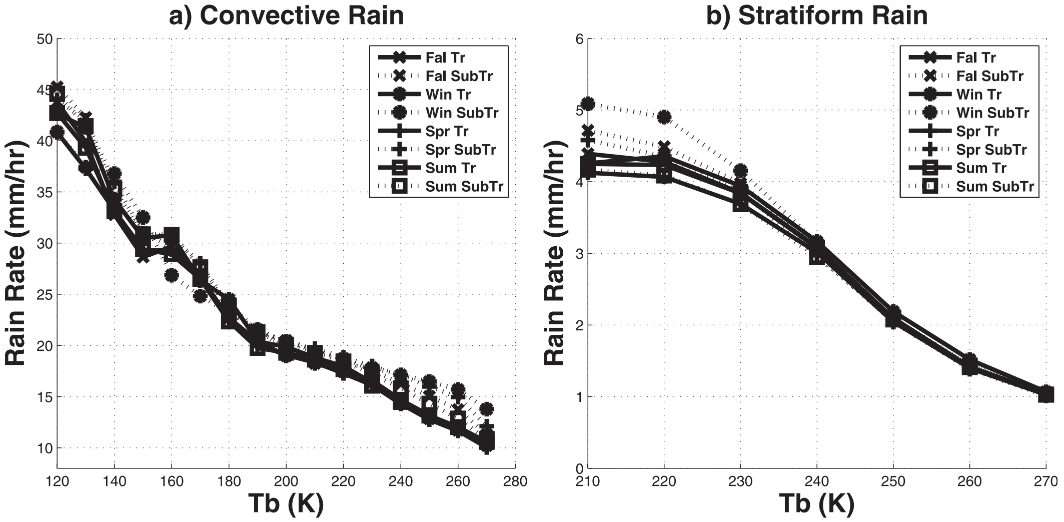

FIG. 3. Mean PR RR for 10-K TMI 85V Tb bins for different seasons and latitude ranges after the filtering technique is applied for (a) convective and (b) stratiform pixels. The RR–Tb relationships for the different regimes are nearly identical after filtering.

where RR_{conv} is the estimated RR for convective pixels, RR_{strat} is the RR estimated from the stratiform profiles, and Tb_{85V} is the 85-GHz vertically polarized channel Tb.

The polynomial fits are extrapolated to estimate RR beyond the 120–270-K Tb range (i.e., RR estimates outside the 1–45 mm h^{-1} range) in rare cases; however, our confidence in these estimates is lower than the confidence in RR estimates between 1 and 45 mm h^{-1}.

c. *Estimation of convective/stratiform ratio for TMI pixels*

The next step in the RR retrieval process requires the estimation of the convective/stratiform percentage for every TMI pixel, in order to account for the coexistence of both convective and stratiform rainfall types in the pixel. The convective and stratiform RR estimates from the TMI 85V Tb for every pixel are combined using the convective probability (ratio) estimate $P(C)$, as described in Eq. (1). The following equation is used to estimate $P(C)$ in TMI v6 (McCollum and Ferraro 2003):

$$\begin{aligned}\mathrm{CPI} = {} & 1.11\mathrm{Tb}_{10\mathrm{V}} - 1.24\mathrm{Tb}_{37\mathrm{V}} + 0.45\mathrm{Tb}_{85\mathrm{V}} - 1.25\mathrm{POL} \\ & + 0.22\mathrm{NPOL} + 1.24\mathrm{STDEV} + 0.14\mathrm{PIWD} - 84.3\end{aligned} \tag{4}$$

$$P(C) = 0.062 + 0.008\,87\mathrm{CPI}, \tag{5}$$

where the Convective Percent Index (CPI) is an intermediate estimator of the TMI convective percentage, Tb_{10V} is the 10-GHz vertically polarized channel Tb, Tb_{37V} is the 37-GHz vertically polarized channel Tb, POL is the difference between the vertical and horizontal polarizations at 85 GHz, NPOL is the normalized polarization difference at 85 GHz (Olson et al. 2001), STDEV is the standard deviation of the 85V Tb in a spatial grid of ≈40 km (Grecu and Anagnostou 2001), and PIWD is the Tb minima method described in Prabhakara et al. (2000).

The distribution of the convective ratio estimate from TMI v6, however, was found to be significantly different from the convective estimate from PR (Awaka et al. 1998) for collocations from January 2002–December 2003, as shown in Fig. 4. In TMI v6, the TMI convective estimate typically had a value of >0.1, even for pixels where PR identified the rain as completely stratiform (such pixels accounted for ≈65% of the collocations). The higher convective estimates in TMI were identified as a major cause of the global "wet" bias in TMI RR retrievals compared to PR, since a small (but significant) weight was being attached to the much larger convective rain estimates even for completely stratiform rain. To better align the global TMI convective estimate distribution with the PR convective estimates, the TMI $P(C)$ for pixels where the TMI v6 convective estimate is less than an empirically derived value α was set to zero. To prevent a gap in the $P(C)$ histogram between 0 and α, the $P(C)$ was modified using the following empirically derived method:

$$P(C)_{\mathrm{v7}} = \begin{cases} 0 & \text{if} \quad P(C)_{\mathrm{v6}} < \alpha, \\ 2[P(C)_{\mathrm{v6}} - \alpha] & \text{if} \quad \alpha \le P(C)_{\mathrm{v6}} < 2\alpha, \\ P(C)_{\mathrm{v6}} & \text{if} \quad P(C)_{\mathrm{v6}} \ge 2\alpha. \end{cases} \tag{6}$$

where $P(C)_{v6}$ is the convective estimate from TMI v6 and $P(C)_{v7}$ is the modified convective estimate used in

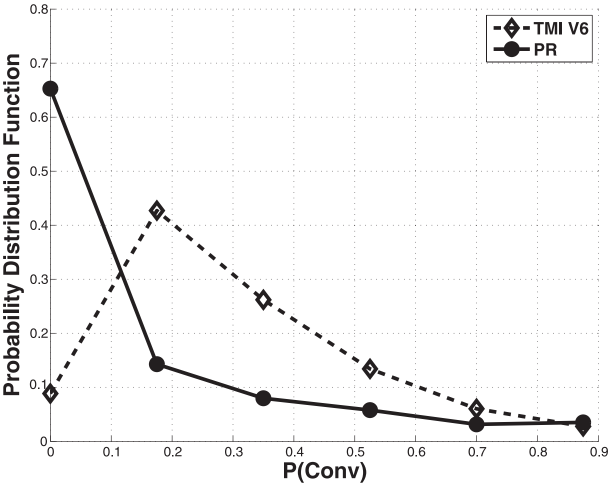

FIG. 4. Comparison of the probability density functions of the convective ratio estimated by TMI v6 and PR. There are significant differences in the convective ratio estimates from TMI and PR.

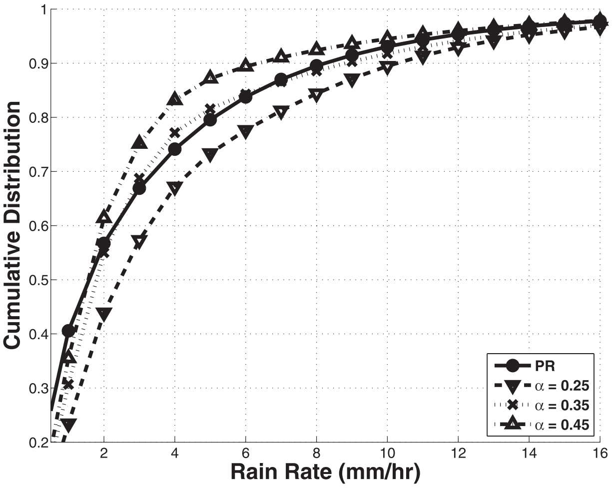

FIG. 5. Comparison of TMI cumulative RR distributions for various values of α with PR for the year 2002; $\alpha = 0.35$ gives the best fit with PR.

the proposed TMI version 7 algorithm. The value of α was empirically optimized by setting different values of α and choosing the value that provided the closest fit between the RR cumulative density functions for TMI and PR (see Fig. 5). The value of $\alpha = 0.35$ was chosen because it resulted in the closest fit between the TMI and PR RR distributions. In comparing the modified TMI convective estimates with PR, it was observed that the distributions of the two convective estimates were extremely similar to each other (see Fig. 6).

The TMI land rainfall described above was validated by making comparisons with PR and GPCC using data from January 2002 to December 2008. The results are presented in the next section.

3. Results

The major goal of the work described in this paper was to reduce the global difference of land rainfall by the TMI land algorithm as compared to PR. To determine the extent to which this objective was achieved, we conducted global statistical RR comparisons of TMI v6 and v7 with reference datasets such as PR and GPCC. We also evaluated the v7 algorithm's performance in retrieving instantaneous RRs by studying a limited number of storm cases.

a. *Evaluation of global TMI rain climatology*

To demonstrate the improvement in the TMI global "wet" bias, the mean global rain rates over land (excluding coast) for TMI v6, TMI v7, and PR from 2002 to 2007 were calculated. The mean global RR for TMI v6 was 2.77 mm day^{-1} while the RR for PR was 2.1 mm day^{-1}; thus, TMI v6 overestimated the mean global RR by more than 30% when compared to PR. In contrast, the mean global RR for TMI v7 was 2.15 mm day^{-1}, which is within 2.5% of the PR RR value. Thus, the global TMI land RR bias is essentially eliminated by the proposed algorithm. Figure 7a shows the unconditional RR bias maps between TMI and PR for both v6 and the proposed algorithm. The proposed model reduces the RR bias from >100 to <50 mm month^{-1} over large sections of South America and central Africa. However, large RR biases of 150 mm month^{-1} and greater remain over the Himalayan mountain ranges and the Gobi Desert.

The reduction in global TMI biases compared to PR demonstrates that the main objective of the v7 algorithm

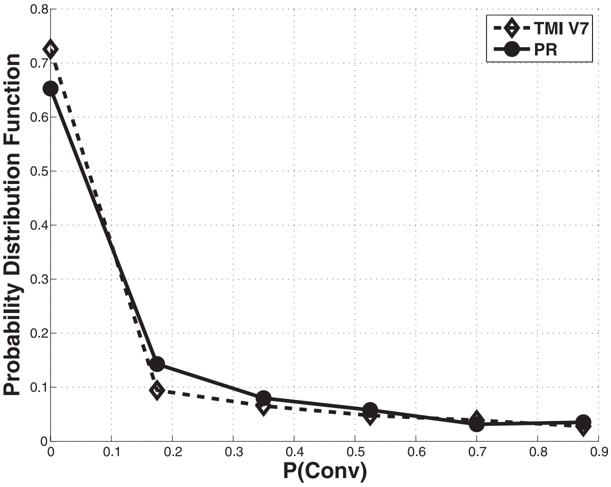

FIG. 6. Comparison of probability density function of TMI v7 convective ratio with PR. The convective ratio in v7 matches PR far more closely than TMI v6.

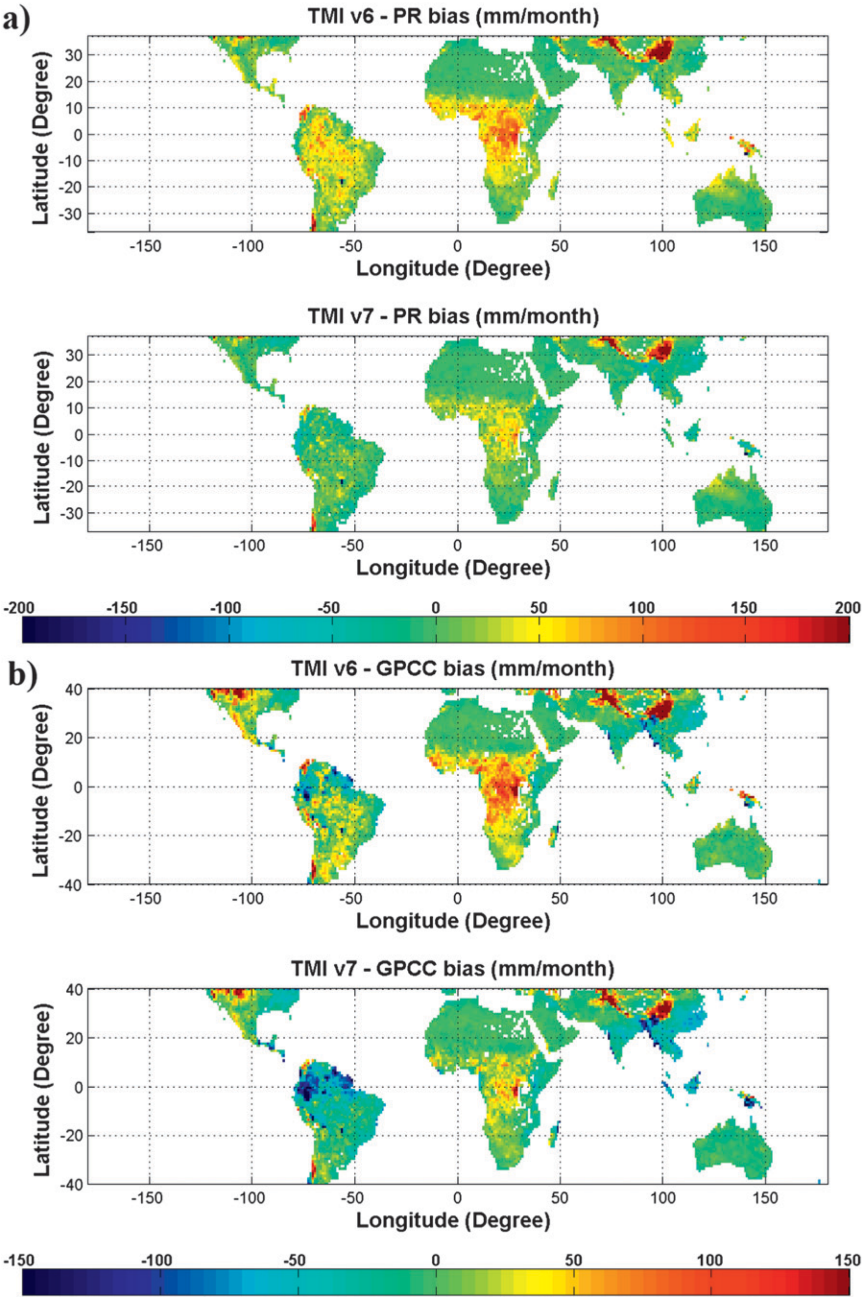

FIG. 7. Global comparisons of TMI v6 and v7 with (a) PR and (b) GPCC. The "wet bias" in TMI v6 is greatly reduced in TMI v7.

has been accomplished to a large degree. However, since the TMI algorithm was trained using PR data, it is important that these results be validated using a data source that is independent from PR. This independent validation was performed by comparing TMI v6 and v7 rain rates with the gridded monthly rain gauge observation data from the GPCC (Schneider et al. 2008). Figure 7b shows a similar pattern of reduction in the TMI biases from v6 to v7 compared to GPCC. TMI v7 detects significantly lower rainfall over the Amazon region as compared to GPCC; this is caused by the fact that PR (which is used to train the TMI algorithm) also underestimates rainfall in these areas.

There are some other areas where TMI underestimates RR compared to both GPCC and PR, primarily over the eastern United States and eastern China. This

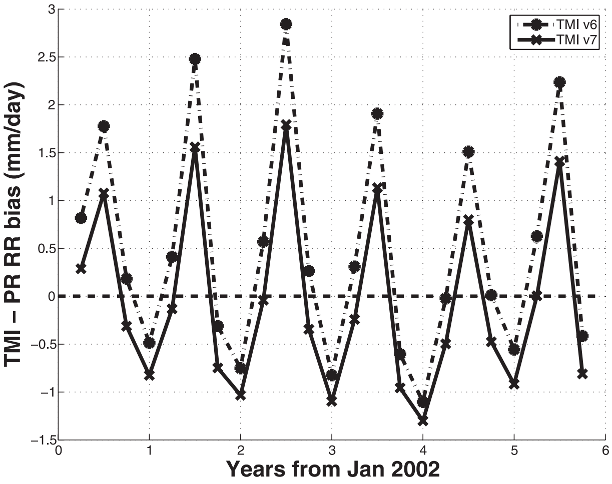

FIG. 8. Seasonal (3 month) averages of the TMI–PR RR bias over the continental United States. The seasonal dependence of the TMI RR biases is essentially unchanged from v6 to v7. However, the overestimation of rainfall in summer is reduced in v7.

negative RR bias is caused primarily by imperfections in the rain/no-rain detection and surface screening procedure in the algorithm (both are unchanged in the new algorithm), which screens the land surfaces such as snow, ice, and desert that exhibit similar scattering signals as the rainfall. Figure 8 shows the 6-yr (2002–07) seasonal averages of the biases for TMI and PR over the continental United States (CONUS). TMI underestimates RR by approximately 0.5 mm day^{-1} or more over the CONUS in the winter (DJF). This is primarily due to conservative screening by the surface screening algorithm, which filters out too many pixels in order to exclude pixels with surface snow and ice, and assigns a zero rain rate for these pixels. Such an underestimation is not seen in the other seasons. It should be noted that the seasonal variability in the TMI bias relative to PR is very similar for v6 and v7, though its amplitude has been reduced to some degree in v7. The elimination of these seasonal bias variations, caused in large measure by surface effects, would require fundamental changes to the screening process in the TMI land algorithm, such as the inclusion of independent water vapor and surface-type data as input. There is also an ongoing effort by many members of the precipitation community to better characterize the variations in land surface emissivity. Developments in this area will likely lead to major improvements in land retrievals from TMI and other passive microwave sensors.

As a result of the reduction in the “wet” bias in TMI, the RR distribution in TMI v7 is significantly closer to

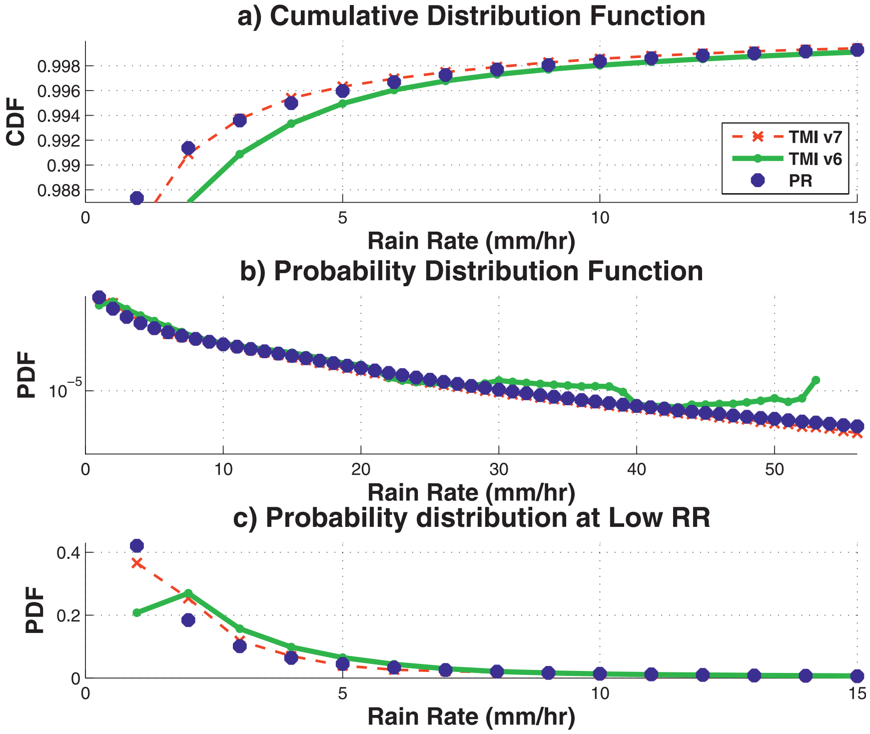

FIG. 9. Comparisons of TMI v6, TMI v7, and PR: (a) cumulative distribution function, (b) probability density function, and (c) probability densities at low RR. TMI v7 matches the PR distribution much better than TMI v6, especially at low RR.

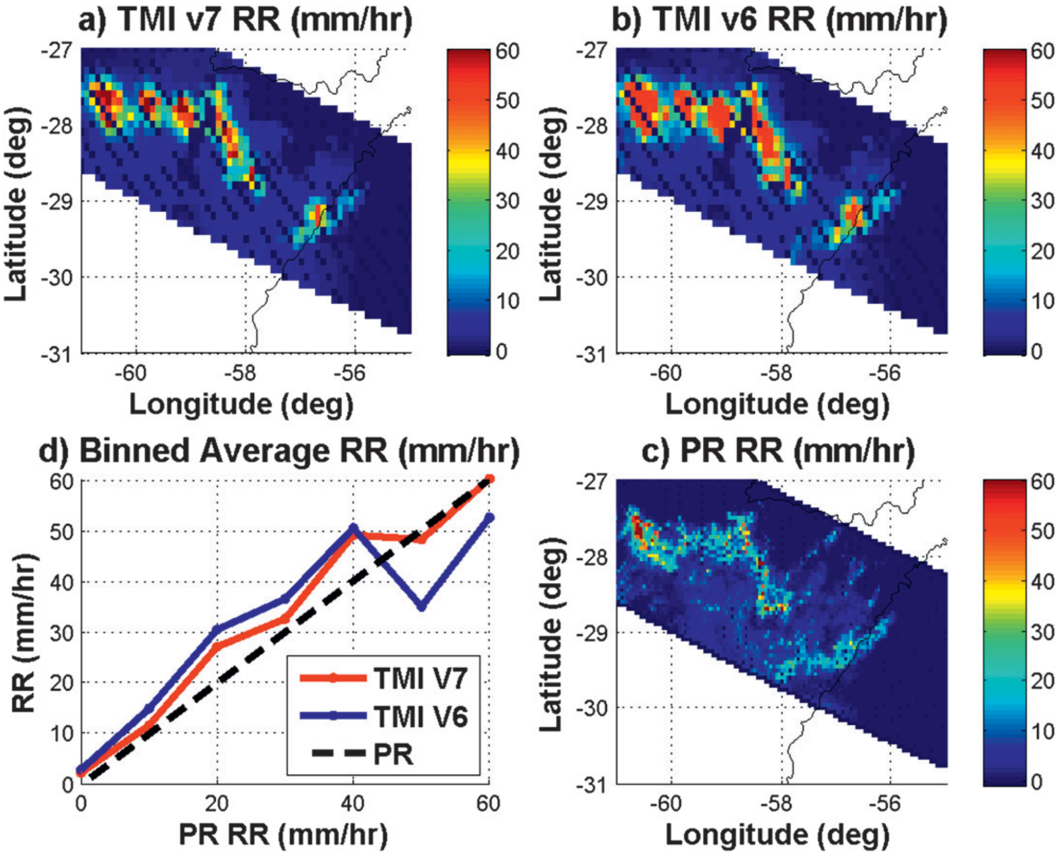

FIG. 10. Case study of MCS over Argentina on 20 Dec 2003 showing (a) TMI v7 RR (mm h^{-1}), (b) TMI v6 RR (mm h^{-1}), (c) PR RR (mm h^{-1}), and (d) binned average. TMI RR for corresponding PR RR bins.

the PR RR distribution than the previous 2A12, land algorithm, as is shown in Fig. 9. In addition, the nonphysical variability in the TMI v6 probability distribution function caused by sampling problems in the Bayesian retrieval that have been eliminated in v7 (see Fig. 9b). The estimates at the low rain rates, which are grossly underestimated by TMI v6, are improved in the new algorithm (see Fig. 9c).

b. *Case studies: TMI rain retrievals for mesoscale convective systems*

The instantaneous rain rates from the TMI algorithm were also validated using a limited number of storm cases. A representative example is shown in Fig. 10, which compares the RR estimates from PR, TMI v6, and the new algorithm for a mesoscale convective system (MCS) over northern Argentina on 20 December 2003 (TRMM orbit 34747). The RR estimates from the new algorithm (see Fig. 10a) have a greater contrast at the highest RRs as compared to the TMI v6 estimates (see Fig. 10b), which saturate at ≈55 mm h^{-1}. Figure 10d shows the binned averages of the TMI RR estimates for 10 mm h^{-1} bins of the corresponding PR RR estimates. In general, the new algorithm is significantly closer to the PR estimates than TMI v6. The mean RR for PR in the raining area is 6.1 mm h^{-1}, TMI v6 retrieves a mean RR of 11.5 mm h^{-1}, and v7 has a mean RR of 9.4 mm h^{-1}. Thus, the v7 algorithm reduces the TMI RR overestimation by almost 40% for this case. Similar results were observed for an MCS over northern Africa on 2 August 2004 (TRMM orbit 38278), as shown in Fig. 11. As with the previous case, TMI v6 RRs are significantly higher than PR, while the v7 RRs are lower than v6, while still being slightly higher than the PR RRs. These case studies demonstrate that the general overestimation of RR by TMI is significantly reduced in v7 for severe convective storms.

4. Conclusions

This paper describes the methodology and the improvements of the new TMI 2A12 land rainfall algorithm. A more robust model of the TMI RR–85V Tb relationship was developed using collocations with TRMM PR from a 7-yr global dataset. The RR–Tb relationships were expressed as a cubic function for convective rain

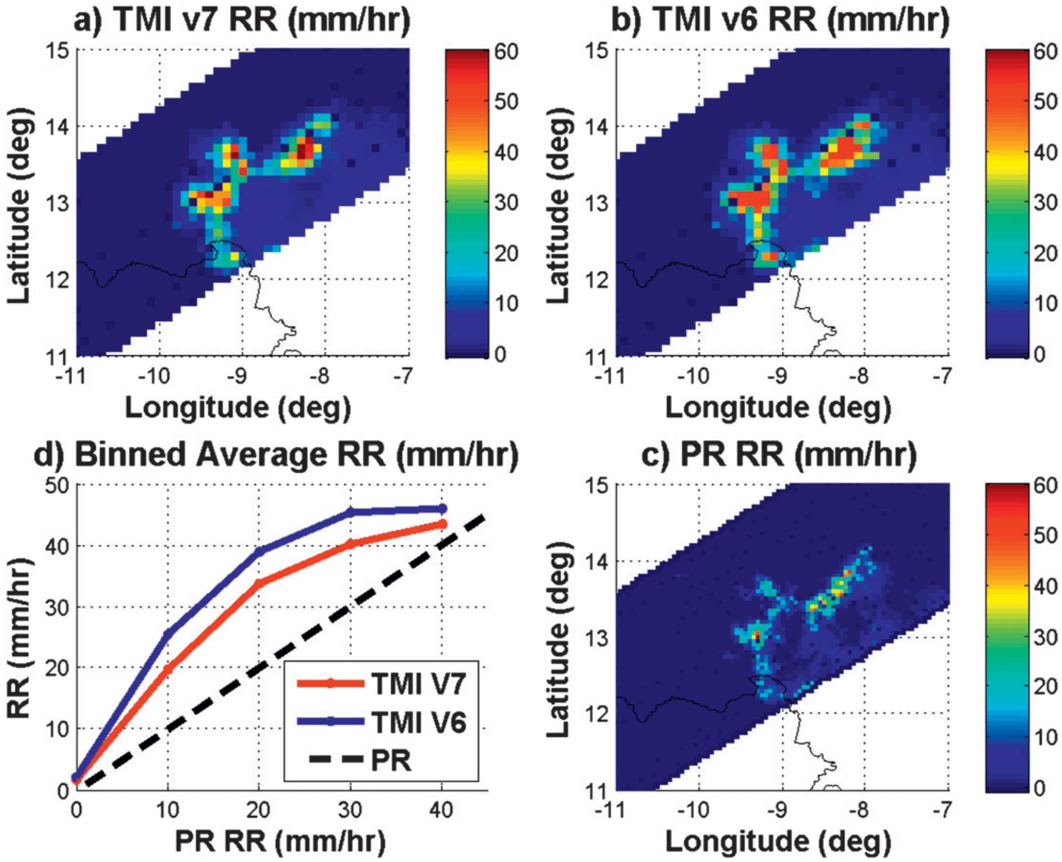

FIG. 11. Case study of MCS over northern Africa on 2 Aug 2004 showing (a) TMI v7 RR (mm h^{-1}), (b) TMI v6 RR (mm h^{-1}), (c) PR RR (mm h^{-1}), and (d) binned average. TMI RR for corresponding PR RR bins.

and a linear function for stratiform rain. Furthermore, the TMI v6 convective fraction estimate was also modified in order to align its distribution more closely with the distribution of the PR convective fraction estimates, which are more reliable. The proposed algorithm results in a drastic reduction in the TMI–PR global mean RR bias. The overestimation of rainfall over central Africa and South America by TMI over PR is also significantly reduced in the new algorithm. The proposed algorithm was also validated using a number of cases, highlighted by observations from a MCS over Argentina, and was found to be closer to the PR RR estimates than TMI v6. Similar results were also observed from an MCS over northern Africa. Additional validation efforts are currently ongoing to validate the performance of the proposed algorithm over different regions and for selected storm cases. The proposed algorithm does not reduce the regional and seasonal dependence of RR biases in TMI estimates, because these dependencies are primarily driven by surface screening, emissivity, warm rainfall, and deep convection. To resolve these issues, we anticipate a thorough review of the TMI land rain detection and screening algorithm. Separate treatments on the deep convection and warm rain cases may be necessary. The collocation technique used to match up TMI and PR pixels will be improved, so that it accounts for the difference in view geometry between TMI and PR, especially for deep convective rainfall. It is also likely that the inclusion of additional rain predictors in addition to the ice scattering signal will be needed. Such an exercise is beyond the scope of this work, and will be undertaken in the near future.

Acknowledgments. The authors would like to acknowledge Professor Ed Zipser at the University of Utah for the use of the precipitation feature data base and the reviewers for making important criticisms and suggestions We are also grateful for the support from NASA (R. Kakar) and NOAA (C. Miller and J. Pereira). This work was partially supported through a grant between NOAA and the University of Maryland/Cooperative Institute for Climate Studies.

REFERENCES

Awaka, J., T. Iguchi, and K. Okamoto, 1998: Early results on rain type classification by the Tropical Rainfall Measuring Mission

(TRMM) precipitation radar. *Proc. Eighth URSI Commission F Open Symp.,* Aveiro, Portugal, URSI, 143–146.

Dinku, T., and E. Anagnostou, 2005: Regional differences in overland rainfall estimation from PR-calibrated TMI algorithm. *J. Appl. Meteor.,* **44,** 189–205.

Ferraro, R., and G. Marks, 1995: The development of SSM/I rain-rate retrieval algorithms using ground-based radar measurements. *J. Atmos. Oceanic Technol.,* **12,** 755–770.

Grecu, M., and E. Anagnostou, 2001: Overland precipitation estimation from TRMM passive microwave observations. *J. Appl. Meteor.,* **40,** 1367–1380.

Grody, N., 1991: Classification of snow cover and precipitation using the Special Sensor Microwave Imager. *J. Geophys. Res.,* **96,** 7423–7435.

Iguchi, T., T. Kozu, R. Meneghini, J. Awaka, and K. Okamoto, 2000: Rain-profiling algorithm for the TRMM Precipitation Radar. *J. Appl. Meteor.,* **39,** 2038–2052.

Kummerow, C., and Coauthors, 2001: The evolution of the Goddard Profiling Algorithm (GPROF) for rainfall estimation from passive microwave sensors. *J. Appl. Meteor.,* **40,** 1801–1820.

Liu, C., and E. Zipser, 2009: ''Warm rain'' in the tropics: Seasonal and regional distributions based on 9 yr of TRMM data. *J. Climate,* **22,** 767–779.

——, ——, D. Cecil, S. Nesbitt, and S. Sherwood, 2008: A cloud and precipitation feature database from nine years of TRMM observations. *J. Appl. Meteor. Climatol.,* **47,** 2712–2728.

McCollum, J., and R. Ferraro, 2003: Next generation of NOAA/NESDIS TMI, SSM/I, and AMSR-E microwave land rainfall algorithms. *J. Geophys. Res.,* **108,** 8382, doi:10.1029/2001JD001512.

Olson, W. S., Y. Hong, C. D. Kummerow, and J. Turk, 2001: A texture-polarization method for estimating convective–stratiform precipitation area coverage from passive microwave radiometer data. *J. Appl. Meteor.,* **40,** 1577–1591.

Prabhakara, C., R. Icovazzi Jr., J. A. Weinman, and G. Dalu, 2000: A TRMM microwave radiometer rain rate estimation method with convective and stratiform discrimination. *J. Meteor. Soc. Japan,* **78,** 241–258.

Schneider, U., T. Fuchs, A. Meyer-Christoffer, and B. Rudolf, 2008: Global Precipitation Analysis Products of the GPCC. Global Precipitation Climatology Centre, DWD, 12 pp. [Available online at ftp://ftp-anon.dwd.de/pub/data/gpcc/PDF/GPCC_intro_products_2008.pdf.]

Wang, N.-Y., C. Liu, R. Ferraro, D. Wolff, E. Zipser, and C. Kummerow, 2009: TRMM 2A12 land precipitation product—Status and future plans. *J. Meteor. Soc. Japan,* **87A,** 237–253.